# *Origin and dynamics of global atmospheric wavenumber-4 in the Southern mid-latitude during austral summer*

Article

Accepted Version

# Origin and dynamics of global atmospheric wavenumber-4 in the Southern mid-latitude during austral summer

**Balaji Senapati[1], Pranab Deb[1], Mihir K. Dash[1], and Swadhin K. Behera[2]**

[1]Centre for Oceans, Rivers, Atmosphere and Land Sciences, Indian Institute of Technology Kharagpur, Kharagpur, West Bengal, India.

[2]Application Laboratory, VAiG, Japan Agency for Marine-Earth Science and Technology, Yokohama, Kanagawa, Japan.

Corresponding author: Mihir K. Dash (mihir@coral.iitkgp.ac.in)

**ORCID**

*Balaji Senapati:* https://orcid.org/0000-0001-5029-9731

*Pranab Deb:* https://orcid.org/0000-0002-1858-0918

*Mihir K. Dash:* https://orcid.org/0000-0003-1426-7200

*Swadhin K. Behera:* https://orcid.org/0000-0001-8692-2388

## Abstract

Using empirical orthogonal function analysis, a stationary atmospheric wavenumber-4 (AW4) pattern is identified in the Southern mid-latitudes during austral summer. The generation mechanism and its linkage to Southern Hemisphere climate is explored using a linear response model and composite analysis. It is found that, AW4 pattern is forced by a Rossby wave source in the upstream region of the upper-tropospheric westerly wave-guide. The vortex stretching associated with the anomalous convection over subtropical western Pacific Ocean (near the New Zealand coast) adjacent to the westerly jet triggers the Rossby wave train around mid-November. This disturbance gets trapped in the Southern Hemisphere westerly jet waveguide and circumnavigates the globe. Around 15-25 days later (in early December), a steady AW4 pattern is established in the Southern mid-latitudes. Further, correlation analysis suggests the AW4 pattern is independent of other natural variabilities such as El Niño/Southern Oscillation, Southern Annular Mode, and Indian Ocean Dipole. The AW4 pattern is found to influence the rainfall over different parts of South America and Australia by modulating upper-level divergence.

**Key words:** Atmospheric barotropic wave, teleconnection, linear response theory, Rossby wave, Southern westerly jet

## 1 Introduction

The intra-seasonal to inter-decadal variabilities in the Southern Hemisphere (SH) atmospheric circulation have been studied extensively using both observations, reanalysis datasets and numerical models (Ghil and Mo 1991; Karoly and Vincent 1998; Kidson 1999; Cai and Watterson 2002; Grimm and Ambrizzi 2009). The Southern Annular Mode (SAM) and the two Pacific South American (PSA) patterns are the dominant modes of variabilities that control the spatio-temporal distribution of temperature, rainfall and sea-ice cover in the SH (Grimm & Ambrizzi 2009; Yuan et al. 2018 and references therein; Kidson 1999; Kiladis & Mo 1998; Kingtse C. Mo & Higgins 1998; Osman & Vera 2020). These modes show close association with ENSO activities (Grimm & Ambrizzi 2009; Mo 2000 and references therein). Indeed, the two PSA patterns, PSA-1 and -2, are associated with ENSO triggered Rossby waves due to anomalous convection over eastern and central Pacific during respective flavours of ENSO events (Mo 2000). These Rossby waves exhibit two distinct wavenumber-3 patterns, which influence several aspects of SH climate, viz., the Antarctic sea ice, South Atlantic SST, and South America climate (Kwok and Comiso 2002; Grimm 2003, 2004; Carvalho et al. 2004; Turner 2004; Rodrigues et al. 2015; Yuan et al. 2018)

Generally, alteration in the subtropical jet due to thermal wind balance and wave mean flow interaction in the westerly jet produces Rossby waves (Hoskins & Karoly 1981). Rossby wave teleconnection are particularly strong in the winter hemisphere as a stronger subtropical westerly jet shifts closer to tropics and gets influenced by the tropical diabatic heating (Hoskins & Ambrizzi 1993). Nevertheless, stationary Rossby waves are also generated in the summer hemisphere, especially in SH, if the source of diabatic heating is located in the vicinity of the subtropical jet (Lee et al. 2009). Numerous studies have identified the presence of mid-latitude wave trains in the SH during austral summer (Jury et al. 1995; Fauchereau et al. 2003; Lin and Li 2012; Zhao et al. 2013; Manhique et al. 2015; Nagaraju et al. 2018; Lin 2019; Senapati et al. 2021). These waves have been linked to the co-variability of southern subtropical Indian and Atlantic Ocean dipoles (Fauchereau et al. 2003), South African flood in 2013 (Manhique et al. 2015), triggering of Madden–Julian Oscillation over tropical western Indian Ocean (Zhao et al. 2013), inter-annual variability of summer rainfall over Madagascar (Jury et al. 1995) & northwest Australia (Lin and Li 2012), South Atlantic-South Indian Ocean pattern (Lin 2019) and a global wavenumber-4 SST pattern (Senapati et al. 2021).

Recently, Lin (2019) reported an atmospheric barotropic wavenumber-4 pattern restricted within the South Atlantic-South Indian Ocean (SASIO) region. In contrast, a circumglobal atmospheric wavenumber-4 (AW4) pattern in the Southern mid-latitudes, extending well into the southern subtropical Pacific Ocean, has been identified by Manhique et al. (2015) in the atmosphere. Also, it is reported that this AW4 has a potential to affect the marine heat waves and cool spells in Tasman Sea (Chiswell 2021) and flood in South Africa (Manhique et al. 2015). Further, Senapati et al. (2021) have shown that a circumglobal wavenumber-4 pattern exists in the southern subtropical sea surface temperature (SST) during austral summer. This circumglobal AW4 pattern was found to show distinct spatial pattern from the SASIO and may exhibits significant covariability among oceanic and atmospheric parameters in the SH (Senapati et al. 2021). While the ocean-atmosphere covariability is ill recognized, the source of the forcing that triggers the AW4 pattern and its location is not well-understood. This study undertakes a thorough investigation of the origin, propagation, and dynamics of this SH circumglobal AW4 pattern which can lead to a significant improvement in the predictability of the SH weather and climate. In other words, we intend to answer the following three questions: (1) What is the dominant circulation anomaly pattern in the southern mid-latitude during austral summer (December-January-February) and its generation mechanism (2) What is/are the source(s) of the disturbance that triggers the circulation, and (3) How it (circulation pattern) impacts the SH weather and climate?

## 2 Data & methods

The dominant inter-annual mode of variability in circulation over Southern mid-latitude (30°S-60°S) is obtained from the Empirical Orthogonal Function (EOF) analysis for meridional wind anomaly. We used daily and monthly atmospheric variables such as wind (both zonal and meridional component at 250, 500 and 850 hPa), geopotential height at 250 , 500 and 850 hPa, and precipitable water at a horizontal resolution of 2.5°x2.5° (from National Centers for Environmental Prediction-2 reanalysis products (Kanamitsu et al. 2002); https://psl.noaa.gov/data/gridded/data.ncep.reanalysis2.html; 2.5°x2.5°), and monthly SST data at a horizontal resolution of 1°x1° (from Hadley Centre Global Sea Ice and Sea Surface Temperature (Rayner et al. 2003); https://www.metoffice.gov.uk/hadobs/hadisst/data/download.html; 1°x1°) during 1979-2018.

Firstly, daily and monthly anomaly of all the variables are calculated at each grid point by removing corresponding annual cycle using equation (1). Afterwards, the time series of each variable is detrended by subtracting corresponding linear trend at each grid point using least square fit. In this method, the cost function of a variable 'S', $S = \sum_{i=1}^{n}\left(y_i - f(x_i)\right)^2$ , is minimized to derive the best fit function, where, $y_i$ is the dependent variable and $x_i$ is the independent variable and $f(x_i)$ is the best fit function. Further, for daily composite analysis, a 90-day low pass filter in the Fourier domain is applied to remove the intra-seasonal oscillation from the daily anomaly time series. Fast Fourier transform converts the time series data into frequency domain using equation (2). High frequencies maximum of 90 days are filtered out from the frequency domain, and then converted back to the time domain using inverse fast Fourier transform.

The monthly/daily anomaly of the monthly/daily time series "$d(t_{i,j})$" at a grid point is calculated by removing its annual cycle "$d(\overline{t_i})$", as follows:

$$d(t'_{i,j}) = d(t_{i,j}) - d(\overline{t_i}) \quad \text{-------------------} \ (1)$$

where, $i$ represents month (January to December) or day (all calendar days) and $j$ represents year (i.e. 1979 to 2018). Prime and over bar represent monthly/daily anomaly and corresponding monthly/daily mean respectively.

The historical time series I(t) measured over the time interval $0 \leq t \leq T$ is transformed into frequency domain $O(\omega, t)$ for all the frequencies '$\omega$' as follows:

$$O(\omega, t) = \int_0^T I(t) e^{-i2\pi\omega t} dt \quad \text{-------------------} \ (2)$$

Further, the co-variability between SASIO and AW4 is analysed using cross-wavelet coherence (Grinsted et al. 2004). Here the coherency of the cross wavelet transform in time-frequency space is measured using equation (8) mentioned in Grinsted et al. (2004). The significance of the wavelet coherence is tested at 5% level using the Monte-Carlo approach (Grinsted et al. 2004).

Following Deb et al. (2020), the semi-empirical linear step response method is adopted to explore the generation and dynamics of the AW4. Here, the extra-tropical response to tropical forcing is assumed to be linear. According to linear response theory, any signal (S) at time 't' can be quantified as the weighted sum of previous forcing (F) of last 'T' days and mean/residual variation:

$$S(t) = \int_0^T G(l) F(t - l) dl + R \quad \text{-------------------} \ (3)$$

Where, $l$ and $R$ represents time lag and residual respectively.

Here, the rainfall anomaly over the western sub-tropical Pacific is taken as forcing F(t) while S(t) represents resultant variables (e.g. geopotential height anomaly, meridional wind etc.) at each grid point over SH (south of equator). 'T' represents the imposed maximum cut off lag. The weights (G's) are calculated using a weighted Quasi-green's functions (Hasselmann et al. 1993) solving equation 3. The elemental assumption in equation (1) is that the southern subtropical atmosphere responds to western subtropical Pacific rainfall anomaly as a linear system, and the former does not exert a large local feedback on the later processes. The impact of other modes of natural variability that influence the southern subtropical atmosphere is captured by the non-negligible residual term R. Multiple linear least square regression method is applied on signal 'S(t)' against lagged rainfall forcing 'F(t)' to calculate the value of impulse response G(*l*) for *l*=0, …, T (for detail method, refer Deb et al. 2020). The step response at any time lag '$l_j$' is computed by using the value of G's in equation (4).

$$S_{step}(l_j) \approx \sum_{i=0}^{j} G(l_i)\Delta l \qquad \text{------------------- (4)}$$

The Rossby wave source (RWS) comprises mainly of two components, (i) the vortex stretching by eddies (S1) and (ii) the advection of absolute vorticity by divergent wind (S2) (Sardeshmukh and Hoskins 1988; Jianchun Qin and Robinson 1993):

$$RWS = -(\xi + f)\,\boldsymbol{\nabla}.\,V\chi - V\chi.\,\boldsymbol{\nabla}(\xi + f) \qquad \text{----------- (5)}$$

Where, $\xi$, f, and $V\chi$ are relative vorticity, planetary vorticity, and irrotational wind respectively.

Different climate indices like Oceanic Niño index (ONI; https://origin.cpc.ncep.noaa.gov) from CPC, NOAA; Pacific Decadal Oscillation index (PDO; https://www.ncdc.noaa.gov) from NCDC, NOAA; Indian Ocean Dipole index (IOD; https://www.esrl.noaa.gov) from ESRL, NOAA; Southern Annular Mode index (SAM; https://climatedataguide.ucar.edu) from NCAR/UCAR are adopted. Indian Ocean Sub-tropical Dipole index (IOSD) (Behera and Yamagata 2001), SST wavenumber-4 index (Senapati et al. 2021), South pacific quadruple index (Ding et al. 2015), El Niño Modoki index (EMI) (Ashok et al. 2007) and South Atlantic Sub-tropical Dipole index (SASD) (Morioka et al. 2011) were calculated to examine their relationship with AW4 index.

Various methods were adopted to test the significance of results in this study. Independency of EOF modes are tested using North criteria (North et al. 1982). North criteria uses the equation (6) to find out the standard error ($\nabla\chi$) of the corresponding eigenvalues ($\chi$) with 'N' degrees of freedom present in the dataset. If the sampling error of a specific eigenvalue '$\chi$' is less than the spacing between $\chi$ and nearest eigenvalue then the EOF associated with $\chi$ is most likely to be independent, else otherwise.

$$\nabla\chi = \chi\left(\frac{2}{N}\right)^{1/2} \qquad \text{------------------- (6)}$$

The significance of Pearson's linear correlation coefficient 'r' is tested against the null hypothesis using t-test statistic, $t=r\times\sqrt{[(n-2)\div(1-r^2)]}$ having student-t distribution of 'n-2' degrees of freedom. For composite analysis, the sample mean ($\bar{x}$) is tested against the population mean (μ) with t-test statistic, $t= (\bar{x}-\mu)/(s/\sqrt{n})$; where, s and n represents sample variance and sample size respectively.

Further, a first order auto-regressive red noise spectrum (AR1) of 1000 samples is used to test the linear step response during austral summer (Deb et al. 2020). An auto-regressive model predicts the next value of a parameter, ($y_{t+1}$), in a time series by regressing with that of current value ($y_t$);

$$y_{t+1} = \alpha \times y_t + F_{std} \times R_n \qquad \text{------------------- (7)}$$

Where, $\alpha$ and $F_{std}$ are the 1st lag auto-correlation and standard deviation of rainfall forcing F(t) respectively. $R_n$ refers to the normalized random numbers which changes in every iteration.

AR1 works as follows: Firstly, AR1 is constructed using equation (7) initialized with the starting value of the rainfall forcing data F(t). Now, actual rainfall forcing data is replaced with AR1 time series in equation (3) to generate a red noise step response at each grid point. This procedure is repeated for 1000 times to give rise to a series of 1000 AR1 step responses at each grid point. Then standard deviation of these 1000 AR1 step response is calculated for each grid point and compared with the actual step response. Finally, the values of actual step response greater than the standard deviation of AR1 step response series is defined as significant.

# 3 Results

## 3.1 AW4 in the SH

In the Southern Hemisphere, two strong jet streams (i) the subtropical westerly jet and (ii) the polar westerly jet exist throughout the year except for the austral summer season. In austral summer, only strong circum-global polar jet exists with its centre over mid latitude (Lin 2019). The westerly jets, due to the wave guide effect, are the plausible pathways for the zonal propagation of Rossby wave train in the Southern Hemisphere (Hoskins & Ambrizzi 1993).

Meridional wind anomaly (V-wind) is suitable in representing the deviations from zonal flow and hence used to identify the Rossby wave trains in the Southern mid-latitude (Wirth et al. 2018; Lin 2019). The first spatial EOF mode of V- wind anomaly (at 250 hPa, derived from NCEP2 reanalysis) over the southern mid-latitude (30°S-60°S) in austral summer (Fig. 1a) clearly shows the presence of wavenumber-4 structure. Eight alternating anomaly centres are separated from each other by 45º along the zonal direction resulting a standing wave of wavelength 90°. The EOF-1 explains 21.5% of the total variance and is well separated from the EOF-2 (14.67% of total variance) as per the North criteria (North et al. 1982). EOF-2 pattern shows the anomalous circulation over the Pacific Ocean, which extends from the south of Australia to the southern tip of South America and then curves towards South America (Fig. not shown). In general, the EOF-2 pattern describes the regional inter-annual variation over Pacific Ocean similar to PSA patterns (Irving and Simmonds 2016). Similar results were also obtained using V-wind from ERA-5 (Fig. 1b). The corresponding principal component (PC1) time series for both the data sets, NCEP2 and ERA5, are shown in figure 1c. A temporal correlation coefficient of 0.99 exists between both the PCs. It is to be mentioned that NCEP2 data have been used for remaining analysis. Corresponding PC-1 time series of NCEP2 (red line in Fig. 1c) is considered as the AW4 index in this study. It is worth mentioning that the loading of V-wind anomaly over the Pacific Ocean is maximum as compared to other regions in EOF-1 (Fig. 1a, b). To understand its role, the AW4 index is correlated with geo-potential height anomaly (shaded) and horizontal wind (vectors) at 250 hPa (Fig.1d). It is to be noted that the correlation vectors presented are structured by the correlation coefficient between AW4 index and meridional wind for Y direction and zonal wind for X direction. It evident that the AW4 index has a strong correlation with the circulation of the wind in association with geopotential height anomaly in the centre of the cells (Fig. 1d). Thus, it can be speculated that the formed AW4 pattern could be the effect of the Rossby wave circumnavigating the globe embedded in the westerly jet (Wirth et al. 2018; Lin 2019).

The vertical distribution of AW4 pattern in the troposphere is presented by correlating the AW4 index with V-wind (Figs. 2a-c) and geopotential height (Figs. 2d-f) at 250, 500, and 850 hPa. Only significant values satisfying 95% confidence interval are shown in the figure 2. In-phase patterns in V-wind (Figs. 2a-c) and geopotential height (Figs. 2d-f) throughout the atmospheric column in the southern mid-latitudes, implies an equivalent barotropic nature of AW4 pattern. It means, the isobaric surfaces are parallel in the AW4 pattern and the pattern remains same for constant depth of the atmospheric fluid in the Southern mid-latitude. Indeed, the barotropic response from a far-field forcing is already mentioned in previous literature (Hoskins & Karoly 1981). Using a threshold value of one standard deviation in the normalized AW4 index, 9 extreme positive (1980, 1985, 1994, 1999, 2002, 2008, 2009, 2013, 2018) and 9 extreme negative (1979, 1983, 1990, 1992, 1993, 2000, 2001, 2007, 2017) years are identified for composite analysis. Remarkably, 50% of SST wavenumber-4 composite years (Senapati et al. 2021) are matching with that of AW4 (4 negative: 1990, 1992, 2000, 2007 and 3 positive: 1980, 1985, and 2018). Also, significant correlation (-0.45 at 99% confidence level) between the two indices (SST wavenumber-4 and AW4) during austral summer, corroborate a strong covariability between atmosphere and ocean. Thus, this study may be helpful to explore and understand the missing link of air-sea coupling that results SST wavenumber-4 pattern (Senapati et al. 2021).

Hovmöller diagram of composite V-wind anomaly for positive AW4 years is constructed by averaging meridionally from 30°S to 60°S (Fig. 3), starting from October of the developing year to the March of the positive event year. The Hovmöller diagram shows that the AW4 is stationary from late November to February (Fig. 3). But before the event, an intrusion of anomalies (i.e. advection of vorticity by the divergent wind anomaly) from the west can be seen between 150°E to 150°W during October and that starts developing in November of the preceding year during positive event years (Fig. 3a). On the other hand, an eastward movement of the anomalies is seen between 150°E to 150°W before developing of AW4 into a mature phase during austral summer in negative event years (Fig. 3b). The weakening of the AW4 pattern in January is also noticed (Fig. 3b) and needed a separate investigation to understand the cause. Nevertheless, it is clear that the forcing for development of AW4 pattern could be present in the subtropical Pacific Ocean for both positive and negative years.

The linkage of AW4 pattern with other known natural climate modes is studied using correlation analysis. Pearson's correlation coefficients of AW4 index with SAM, ONI, IOD, PDO, IOSD, AOSD, EMI and SPQI are 0.2, -0.24, 0.15, 0.01, -0.03, 0.19, -0.2 and 0.01 respectively. The significances of these correlation coefficients are tested against two tailed t-test and found to be insignificant at 90% confidence interval. They suggest, the AW4 pattern is largely independent of these climate phenomena and hence taken for a detailed investigation here.

## 3.2 Dynamics of AW4

The southern mid-latitude is capable of retaining Stationary Rossby waves (of wavenumbers 3-6) develop in the SH within 15-20 days of the initiation of the disturbance, and are confined within the westerly jet wave-guide (Hoskins and Ambrizzi 1993; Ambrizzi et al. 1995). To uncover the underlying mechanism of AW4, a daily composite of detrended and filtered 250 hPa geopotential height and horizontal wind anomalies for the positive years are shown at 15 days interval (Figs. 4a-d). During early November, three cells are observed in the geopotential height and wind in the western Pacific, spreading from tropics to high latitude (Fig. 4a). Subsequently, strong advection of positive geopotential anomaly from south of Australia along with a global wavenumber-3 pattern is observed in mid-November (Fig. 4b). Nearly a fortnight later (during late November) an enhancement positive geopotential height anomaly formed over western Pacific (off-shore of New Zealand) with a well-developed global AW4 pattern (Fig. 4c). Now the AW4 pattern is accompanied with the positive SST anomaly during November over western subtropical Pacific (Fig. 4e) that leads to the Wavenumber-4 pattern in SST anomaly later in the season (Senapati et al. 2021).

Development of positive geopotential height anomaly over western subtropical Pacific near New Zealand in mid-November disturbs the atmospheric circulation. Eventually, the disturbance propagates eastward guided by the westerly waveguide and an AW4 pattern is formed in geopotential height anomaly and related circulation in the southern mid-latitude. Overall, the signal takes around 15-25 days to circumnavigate the globe and develop into a well-established AW4 stationary pattern by early December (Fig. 4d), and strengthens gradually.

The source of the disturbance is investigated using composites of precipitable water and upper-level divergence (Fig. 4f). Favouring to previous result (Figs. 4a-d), positive precipitation anomaly and divergence during positive AW4 years suggests presence of a diabatic source over western subtropical Pacific. However, simultaneous occurrence of enhanced precipitations over some other regions like Maritime Continent and South Africa leaves us with some ambiguity of the exact source of the AW4 forcing. To avoid this confusion Rossby wave source is identified using equation (5), consisting mainly of vortex stretching (first term ($S_1$)) and advection of absolute vorticity by divergent wind (second term ($S_2$)). The correlation map between AW4 index and RWS (Fig. 5a) clearly depicts three regions in the subtropical Pacific Ocean as the possible source for trigging the AW4 pattern, predominantly due to the vortex stretching (Fig. 5b). Vortex stretching term in RWS (Fig. 5b) represents exactly the same as RWS (Fig. 5a). On the other hand, advection of absolute vorticity by divergent wind in RWS are found over the southwest part of the western Pacific (shown by the blue box in fig. 5a) and near western Antarctic continent (Fig. 5c). But, these regions don't contribute to RWS (Fig. 5a) and the region near western Antarctic continent is most probably due to the downstream effect of the Rossby wave.

The Rossby wave train propagates eastward in the SH westerly waveguide and hence the wave pattern is most likely forced by a RWS present in the upstream region of the jet. A close inspection of figures 4 and 5 indicates that the region with strong Rossby wave activity, near the entrance of the westerly jet over western subtropical Pacific Ocean (160°E-177°E, 30°S-48°S), is the most probable forcing region. During negative years the scenario is apparently opposite (Figs. 4g-j) where the diabatic heating source and associated upper-level divergence (convergence) lies in the eastern (western) subtropical Pacific Ocean (Fig. 4*l*) accompanied by positive (negative) SST anomaly (Fig. 4k). Diabatic heating in the eastern subtropical Pacific Ocean in association with positive SST anomaly there gives rise to a nearby diabatic sink region accompanied with negative SST anomaly over the western side of the subtropical Pacific Ocean. This situation accommodate the negative geopotential height to strengthen over the subtropical Pacific Ocean which perturbs the atmospheric circulation. Afterwards, this disturbance gets trap in the nearby westerly jet to form AW4 pattern seen in negative years.

In the following sub-section, we use the Linear Response Theory to further corroborate this hypothesis that the RWS located over the western subtropical Pacific Ocean (160°E-177°E, 30°S-48°S) is the most important source of the AW4 forcing.

### 3.3 Extratropical Linear response to subtropical RWS

Extratropical linear response due to a RWS placed over western subtropical Pacific (160°E-177°E, 30°S-48°S) can be captured using a linear step response model (Deb et al. 2020). This model provides the response over SH extra-tropics due to a step like change in precipitation/convection over the RWS region. At any time-lag '*l*', the cumulative response can be calculated using equation (4) for a unit 'step-like' change in the forcing parameter. Considering the presence of AW4 pattern in austral summer, daily meridional wind, geopotential height, precipitable water (mm/day), divergence ($s^{-1}$), and 500 hPa vertical wind (pascal/sec) for December-February season are selected as response data, whereas, precipitation anomaly over western subtropical Pacific (probable source of RWS) from October to February is considered as forcing data. It is to be noted that precipitation anomaly for extra two months (October - November) are considered to provide the lead forcing in the model. Eventually, the model is forced by a precipitation anomaly of 3 mm/day over the RWS region in the western Pacific Ocean adjacent to New Zealand coast (shown by the blue box in fig. 5) and the step response (averaged over 30-40 days) is recorded in meridional-wind anomaly at 250hPa (Fig. 6a) and geopotential height anomaly at 250hPa (Fig. 6b). 200hPa V-wind and geopotential height are significant over the southern mid-latitude, suggesting an AW4 pattern similar to the pattern seen in the NCEP2 data (Fig. 1a & 4). Locations of anomalous centers of geopotential height and V-wind clearly represent the formation of 8 anomalous circulation cells accompanying AW4 pattern in the geopotential height anomalies in the mid-latitude belt. Thus, it can be inferred that the AW4 is triggered by anomalous convection over the western subtropical Pacific Ocean, off the New Zealand coast. The diabatic heating, upper-level divergence and vortex stretching associated with this anomalous convection causes a Rossby wave response in the upper atmosphere which assumes a quasi-stationary wavenumber 4 structure within ~15-25 days. The AW4 pattern eventually gets trapped in the westerly waveguide in the SH, and becomes a potential source of atmosphere-ocean variability in the SH.

### 3.4 Effect of AW4 on SH precipitation variability

Inter-annual rainfall variability over South America and Australia are strongly affected by PSA and SASIO patterns in the SH (Grimm 2003, 2004; Grimm and Ambrizzi 2009; Cai et al. 2011; Lin and Li 2012; Yuan et al. 2018; Lin 2019). Remarkably, existence of AW4 over the southern subtropics have also the potential to affect SH continental rainfall. Linear step response (Figs. 6c-e) and composite maps (Figs. 6f-h) shows the impact of AW4 on precipitation over Australia and South America (Figs. 6c and 6f). To identify the physical mechanism linking the AW4 pattern and the continental rainfall (Figs. 6c & 6f), linear step response (similar to figure 6a) and composite maps of positive years are constructed for 250 hPa divergence and 500 hPa vertical motion (Figs. 6d-e & 6g-h) during austral summer season. A significant upper level divergence (Figs. 6d & 6g) and mid tropospheric vertical motion (Figs. 6e & 6h) can be noticed over South America and Australia which are consistent with the rainfall patterns (Figs. 6c & 6f). A horseshoe shaped convergence pattern is observed in the upper troposphere (Fig. 6g) over southern part of South America, associated with a similar structure of descending motion of air (Fig. 6h). This signifies an active sink region over southern South America, marked by a negative precipitation anomaly (Fig. 6f) over that region. Anomalous circulation caused by AW4 pattern causes a northward (southward) meridional wind in the upper level over the South America (western Atlantic Ocean) during positive years (Fig. 6a). As a consequence of zonal gradient in 250 hPa meridional wind, the upper level wind converges over the region and can be witnessed in figures 6d-e & 6g-h. Upper level convergence favours the air to sink and supress the rainfall (Figs. 6c & 6f) over the South America. Notably, the origin of SASIO pattern is related to upper level divergence owing to local rainfall anomalies over mid-latitude South America and southwest South Atlantic. Hence, the covariability between SASIO and AW4 pattern is examined using wavelet coherence (Grinsted et al. 2004). The wavelet coherence pretty well shows an insignificant covariability between them except for two years, 1990-91 & 2012-13 (Fig. S1b). Further, statistically insignificant correlation (0.38; at 99% confidence level) between PC's of AW4 and SASIO, approximately 20° phase difference between their loading centers (Fig. S1a) and different sources of forcing (i.e. different RWS) confirm the distinct nature of AW4 from the SASIO pattern. Further, a dipole type precipitation variability accompanied by upper-level divergence/convergence and vertical motion is also noticed in south-eastern and north-western part of Australia (Figs. 6c and 6f). A local upper tropospheric circulation change due to AW4 pattern (Figs. 6a & 4c-d) initiates a similar mechanism to that of South America, which affects the rainfall over the Australia. The anomalous circulation forced by AW4 activity causes an upper-level convergence (divergence) associated with descending (ascending) air motion (Figs. 6d-e & 6g-h) which acts to supress (enhance) rainfall over the south-eastern (north-western) part of Australia (Figs. 6c & 6f). Notably, lower-level circulation change coupled with local SST variation can also affect the rainfall over south-eastern Australia (Senapati et al. 2021). The scenario is opposite during negative years. Hence, the anomalous circulation generated due to AW4 activity over the Australia and South America affects the weather over the region (Fig. 6c-e). The persistence of the AW4 throughout the season (probably due to the thermodynamic coupling with SST (Senapati et al. 2021)) also affect the seasonal rainfall over the Australia and South America. It can be also noted that, "2013" is a positive extreme AW4 event and matches well with the local circulation changes around South Africa (Figure not shown) during January, 2013 flood (Manhique et al. 2015). Thus, this study can be helpful in understanding such dynamics and teleconnection to improve the short-range to seasonal forecast of SH climate.

## 4 Discussion and Conclusion

Climate of SH is modulated by several high-latitude modes of variability, e.g., SAM, ACW, AO etc., which are characterised by variations in ocean, sea ice and atmosphere (White and Peterson 1996; Gong and Wang 1999; Hall and Visbeck 2002; Wang 2010; Deb et al. 2017). Recently, a circumglobal wavenumber-4 pattern was discovered in the Southern Ocean SST during austral summer (Senapati et al. 2021). It was noted that the SST wave pattern is forced by the atmosphere and sustained for ~3-4 months through a strong thermodynamic coupling. However, the origin and dynamics of the atmospheric wave that forces the ocean to generate the oceanic wave pattern remained unclear.

Here, we demonstrate that a stationary global AW4 in the SH during austral summer responsible for modulating SH climate. Using composite analysis and linear response theory, we show that this stationary AW4 pattern is forced by a RWS in the upstream region of the upper-tropospheric westerly wave-guide. The RWS is maintained by anomalous convection and diabatic heating over the western subtropical Pacific Ocean (adjacent to the New Zealand coast), which triggers a Rossby wave response in the upper troposphere through upper level divergence and vortex stretching. The Rossby wave moves poleward, gets trapped in the westerly wave guide and subsequently attains a quasi-stationary structure within ~15-25 days. However, a weak signal is noticed over Indo-Atlantic region as compared to Pacific Ocean (Fig. 1 & 2). This needs to be investigated with coupled ocean-atmosphere model experiments and will be addressed in a future study. Moreover, a lagged correlation analysis is performed between SST wavenumber-4 index and 850 hPa wind anomalies to identify the source of atmospheric wave that yields to SST wavenumber-4 (Senapati et al. 2021). Figure 7 suggests the anomalous circulation over the RWS region near coastal New Zealand leads the SST wavenumber-4 index by up to 3 months implying that the RWS over coastal New Zealand is instrumental in the generation of SST wavenumber-4 pattern via thermodynamic air-sea coupling with AW4 as discussed in the recent study (Senapati et al. 2021). This thermodynamic air-sea coupling further helps in sustaining the AW4 pattern for months.

Our study shows that precipitation anomalies over SH continents are strongly modulated by AW4 pattern, e.g., the positive phase of AW4 pattern is associated with a dipole-like precipitation anomaly over Australia (with enhanced and suppressed precipitation over north-western and south-eastern part, respectively), and an increased precipitation (associated with a horseshoe-like upper level divergence) over southern part of South America. Moreover, Senapati et al. (2021) showed that the lower-level circulation change coupled with local SST variation forced by AW4 can also affect the rainfall over southeastern Australia. Interestingly, Manhique et al. (2015) suggested a link between 2013 South Africa flood with an atmospheric wavenumber–4 pattern in the SH. Their wavenumber-4 pattern shows close resemblance to the composite atmospheric circulation anomaly during 'extreme' AW4 years (defined as AW4 index greater than one standard deviation, figure not shown) suggesting that January, 2013 flood in South Africa may be attributed to the global AW4 pattern reported here.

Our study makes the first attempt to understand the origin and dynamics of the recently discovered wavenumber-4 teleconnection pattern in the SH which can greatly improve the seasonal-scale predictability of extreme events like floods and droughts. However, the interaction of AW4 with SASIO pattern (Lin 2019) and mid-tropospheric semi-permanent subtropical anticyclones (Reason 2016) remains to be explored.

## Acknowledgements

The first author is thankful to the Department of Science and Technology, New Delhi for funding his research through the INSPIRE PhD fellowship programme (IF170092). The authors are also grateful to the Indian Institute of Technology Kharagpur for providing necessary facilities. NCAR Command Language, Climate Data Operator, Python and Matlab have been used for the analysis. Figures are plotted using PyFerret and Matlab.

## Declarations

### Data availability

All the data that support the findings of this study are available in Kanamitsu et al. (2002) and Rayner et al. (2003). These datasets are openly accessible in respected sites mentioned in the manuscript.

### Code availability

All codes used to perform the analyses in this study are available on request from the corresponding author.

### Conflicts of interest

The authors declare no conflict of interests.

## References

Ambrizzi T, Hoskins BJ, Huang-Hsiung Hsu (1995) Rossby wave propagation and teleconnection patterns in the austral winter. J Atmos Sci. https://doi.org/10.1175/1520-0469(1995)052<3661:RWPATP>2.0.CO;2

Ashok K, Behera SK, Rao SA, et al (2007) El Niño Modoki and its possible teleconnection. J Geophys Res Ocean 112:. https://doi.org/10.1029/2006JC003798

Behera SK, Yamagata T (2001) Subtropical SST dipole events in the southern Indian Ocean. Geophys Res Lett 28:327–330. https://doi.org/10.1029/2000GL011451

Cai W, van Rensch P, Cowan T, Hendon HH (2011) Teleconnection pathways of ENSO and the IOD and the mechanisms for impacts on Australian rainfall. J Clim. https://doi.org/10.1175/2011JCLI4129.1

Cai W, Watterson IG (2002) Modes of interannual variability of the Southern Hemisphere circulation simulated by the CSIRO climate model. J Clim. https://doi.org/10.1175/1520-0442(2002)015<1159:MOIVOT>2.0.CO;2

Carvalho LMV, Jones C, Liebmann B (2004) The South Atlantic convergence zone: Intensity, form, persistence, and relationships with intraseasonal to interannual activity and extreme rainfall. J Clim 17:. https://doi.org/10.1175/1520-0442(2004)017<0088:TSACZI>2.0.CO;2

Chiswell SM (2021) Atmospheric wavenumber-4 driven South Pacific marine heat waves and marine cool spells. Nat Commun 12:. https://doi.org/10.1038/s41467-021-25160-y

Deb P, Dash MK, Dey SP, Pandey PC (2017) Non-annular response of sea ice cover in the Indian sector of the Antarctic during extreme SAM events. Int J Climatol 37:. https://doi.org/10.1002/joc.4730

Deb P, Matthews AJ, Joshi MM, Senior N (2020) The Extratropical Linear Step Response to Tropical Precipitation Anomalies and Its Use in Constraining Projected Circulation Changes under Climate Warming. J Clim 33:7217–7231. https://doi.org/10.1175/JCLI-D-20-0060.1

Ding R, Li J, Tseng Y heng (2015) The impact of South Pacific extratropical forcing on ENSO and comparisons with the North Pacific. Clim Dyn. https://doi.org/10.1007/s00382-014-2303-5

Fauchereau N, Trzaska S, Richard Y, et al (2003) Sea-surface temperature co-variability in the southern Atlantic and Indian Oceans and its connections with the atmospheric circulation in the Southern Hemisphere. Int J Climatol 23:663–677. https://doi.org/10.1002/joc.905

Ghil M, Mo K (1991) Intraseasonal Oscillations in the Global Atmosphere. Part2: Southern Hemisphere. J. Atmos. Sci.

Gong D, Wang S (1999) Definition of Antarctic oscillation index. Geophys Res Lett. https://doi.org/10.1029/1999GL900003

Grimm AM (2004) How do La Niña events disturb the summer monsoon system in Brazil? Clim Dyn 22:. https://doi.org/10.1007/s00382-003-0368-7

Grimm AM (2003) The El Niño impact on the summer monsoon in Brazil: Regional processes versus remote influences. J Clim 16:. https://doi.org/10.1175/1520-0442(2003)016<0263:TENIOT>2.0.CO;2

Grimm AM, Ambrizzi T (2009) Teleconnections into South America from the Tropics and Extratropics on Interannual and Intraseasonal Timescales

Grinsted A, Moore JC, Jevrejeva S (2004) Application of the cross wavelet transform and wavelet coherence to geophysical time series. Nonlinear Process Geophys 11:. https://doi.org/10.5194/npg-11-561-2004

Hall A, Visbeck M (2002) Synchronous variability in the Southern Hemisphere atmosphere, sea ice, and ocean resulting from the annular mode. J Clim 15:. https://doi.org/10.1175/1520-0442(2002)015<3043:SVITSH>2.0.CO;2

Hasselmann K, Sausen R, Maier-Reimer E, Voss R (1993) On the cold start problem in transient simulations with coupled atmosphere-ocean models. Clim Dyn. https://doi.org/10.1007/BF00210008

Hoskins BJ, Ambrizzi T (1993) Rossby wave propagation on a realistic longitudinally varying flow. J. Atmos. Sci. 50:1661–1671

Irving D, Simmonds I (2016) A new method for identifying the Pacific-South American pattern and its influence on regional climate variability. J Clim 29:. https://doi.org/10.1175/JCLI-D-15-0843.1

Jianchun Qin, Robinson WA (1993) On the Rossby wave source and the steady linear response to tropical forcing. J Atmos Sci. https://doi.org/10.1175/1520-0469(1993)050<1819:otrwsa>2.0.co;2

Jury MR, Parker BA, Raholijao N, Nassor A (1995) Variability of summer rainfall over Madagascar: Climatic determinants at interannual scales. Int J Climatol. https://doi.org/10.1002/joc.3370151203

Kanamitsu M, Ebisuzaki W, Woollen J, et al (2002) NCEP-DOE AMIP-II reanalysis (R-2). Bull Am Meteorol Soc 83:. https://doi.org/10.1175/bams-83-11-1631

Karoly DJ, Vincent DG (1998) Meteorology of the Southern Hemisphere. Meteorol Monogr. https://doi.org/10.1175/0065-9401-27.49.1

Kidson JW (1999) Principal modes of Southern Hemisphere low-frequency variability obtained from NCEP-NCAR reanalyses. J Clim. https://doi.org/10.1175/1520-0442(1999)012<2808:PMOSHL>2.0.CO;2

Kiladis GN, Mo KC (1998) Interannual and Intraseasonal Variability in the Southern Hemisphere. In: Meteorology of the Southern Hemisphere

Kwok R, Comiso JC (2002) Southern Ocean climate and sea ice anomalies associated with the Southern Oscillation. J Clim 15:. https://doi.org/10.1175/1520-0442(2002)015<0487:SOCASI>2.0.CO;2

Lin Z (2019) The South Atlantic-South Indian ocean pattern: A zonally oriented teleconnection along the Southern Hemisphere westerly jet in austral summer. Atmosphere (Basel) 10:. https://doi.org/10.3390/atmos10050259

Lin Z, Li Y (2012) Remote influence of the tropical Atlantic on the variability and trend in North West Australia summer rainfall. J Clim. https://doi.org/10.1175/JCLI-D-11-00020.1

Madden RA, Julian PR (1994) Observations of the 40-50-day tropical oscillation - a review. Mon Weather Rev. https://doi.org/10.1175/1520-0493(1994)122<0814:OOTDTO>2.0.CO;2

Manhique AJ, Reason CJC, Silinto B, et al (2015) Extreme rainfall and floods in southern Africa in January 2013 and associated circulation patterns. Nat Hazards. https://doi.org/10.1007/s11069-015-1616-y

Mo KC (2000) Relationships between low-frequency variability in the Southern Hemisphere and sea surface temperature anomalies. J Clim. https://doi.org/10.1175/1520-0442(2000)013<3599:RBLFVI>2.0.CO;2

Mo KC, Higgins RW (1998) The Pacific-South American modes and tropical convection during the Southern Hemisphere winter. Mon Weather Rev. https://doi.org/10.1175/1520-0493(1998)126<1581:TPSAMA>2.0.CO;2

Morioka Y, Tozuka T, Yamagata T (2011) On the growth and decay of the subtropical dipole mode in the South Atlantic. J Clim 24:5538–5554. https://doi.org/10.1175/2011JCLI4010.1

Nagaraju C, Ashok K, Balakrishnan Nair TM, et al (2018) Potential influence of the Atlantic Multi-decadal Oscillation in modulating the biennial relationship between Indian and Australian summer monsoons. Int J Climatol 38:. https://doi.org/10.1002/joc.5722

North GR, Bell TL, Cahalan RF, Moeng FJ (1982) Sampling Errors in the Estimation of Empirical Orthogonal Functions. Mon Weather Rev. https://doi.org/10.1175/1520-0493(1982)110<0699:seiteo>2.0.co;2

Nuncio M, Yuan X (2015) The influence of the Indian Ocean dipole on Antarctic sea ice. J Clim. https://doi.org/10.1175/JCLI-D-14-00390.1

Osman M, Vera CS (2020) Predictability of extratropical upper-tropospheric circulation in the Southern Hemisphere by its main modes of variability. J Clim. https://doi.org/10.1175/JCLI-D-19-0122.1

Rayner NA, Parker DE, Horton EB, et al (2003) Global analyses of sea surface temperature, sea ice, and night marine air temperature since the late nineteenth century. J Geophys Res Atmos. https://doi.org/10.1029/2002jd002670

Reason CJC (2016) The Bolivian, Botswana, and Bilybara Highs and Southern Hemisphere drought/floods. Geophys Res Lett 43:1280–1286. https://doi.org/10.1002/2015GL067228

Rodrigues RR, Campos EJD, Haarsma R (2015) The impact of ENSO on the south Atlantic subtropical dipole mode. J Clim 28:. https://doi.org/10.1175/JCLI-D-14-00483.1

Sardeshmukh PD, Hoskins BJ (1988) The generation of global rotational flow by steady idealized tropical divergence. J Atmos Sci. https://doi.org/10.1175/1520-

0469(1988)045<1228:TGOGRF>2.0.CO;2

Senapati B, Dash MK, Behera SK (2021) Global wave number-4 pattern in the southern subtropical sea surface temperature. Sci Rep 11:1–12. https://doi.org/10.1038/s41598-020-80492-x

Turner J (2004) The El Niño-Southern Oscillation and Antarctica. Int J Climatol 24:. https://doi.org/10.1002/joc.965

Wang F (2010) Subtropical dipole mode in the Southern Hemisphere: A global view. Geophys Res Lett 37:1–4. https://doi.org/10.1029/2010GL042750

White WB, Peterson RG (1996) An Antarctic circumpolar wave in surface pressure, wind, temperature and sea-ice extent. Nature. https://doi.org/10.1038/380699a0

Wirth V, Riemer M, Chang EKM, Martius O (2018) Rossby wave packets on the midlatitude waveguide-A review. Mon. Weather Rev.

Yuan X (2004) ENSO-related impacts on Antarctic sea ice: A synthesis of phenomenon and mechanisms. Antarct Sci. https://doi.org/10.1017/S0954102004002238

Yuan X, Kaplan MR, Cane MA (2018) The interconnected global climate system-a review of tropical-polar teleconnections. J. Clim.

Zhao C, Li T, Zhou T (2013) Precursor signals and processes associated with MJO initiation over the tropical indian ocean. J Clim. https://doi.org/10.1175/JCLI-D-12-00113.1

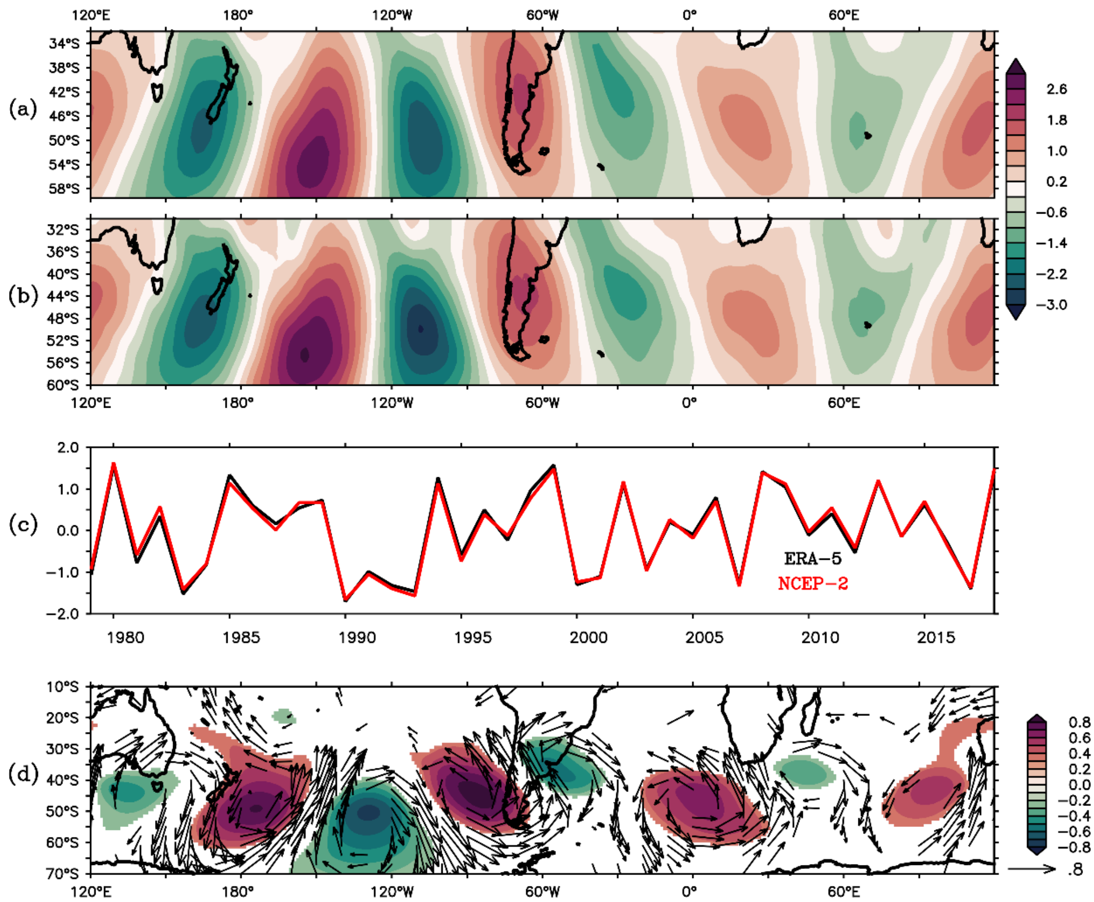


**Fig. 1** Leading EOF mode of 250 hPa meridional wind anomaly over Southern mid-latitude during austral summer (December-January-February mean) for **(a)** NCEP-2 data, **(b)** ERA-5 data. **(c)** Time series of EOF-1 pattern. Solid red (black) line is for NCEP-2 data (ERA-5 data). **(d)** Correlation field of AW4 index with geo-potential height anomaly (filled) and horizontal wind (vectors) at 250 hPa. Values not satisfying 95% confidence using two tailed student's t-test are supressed.

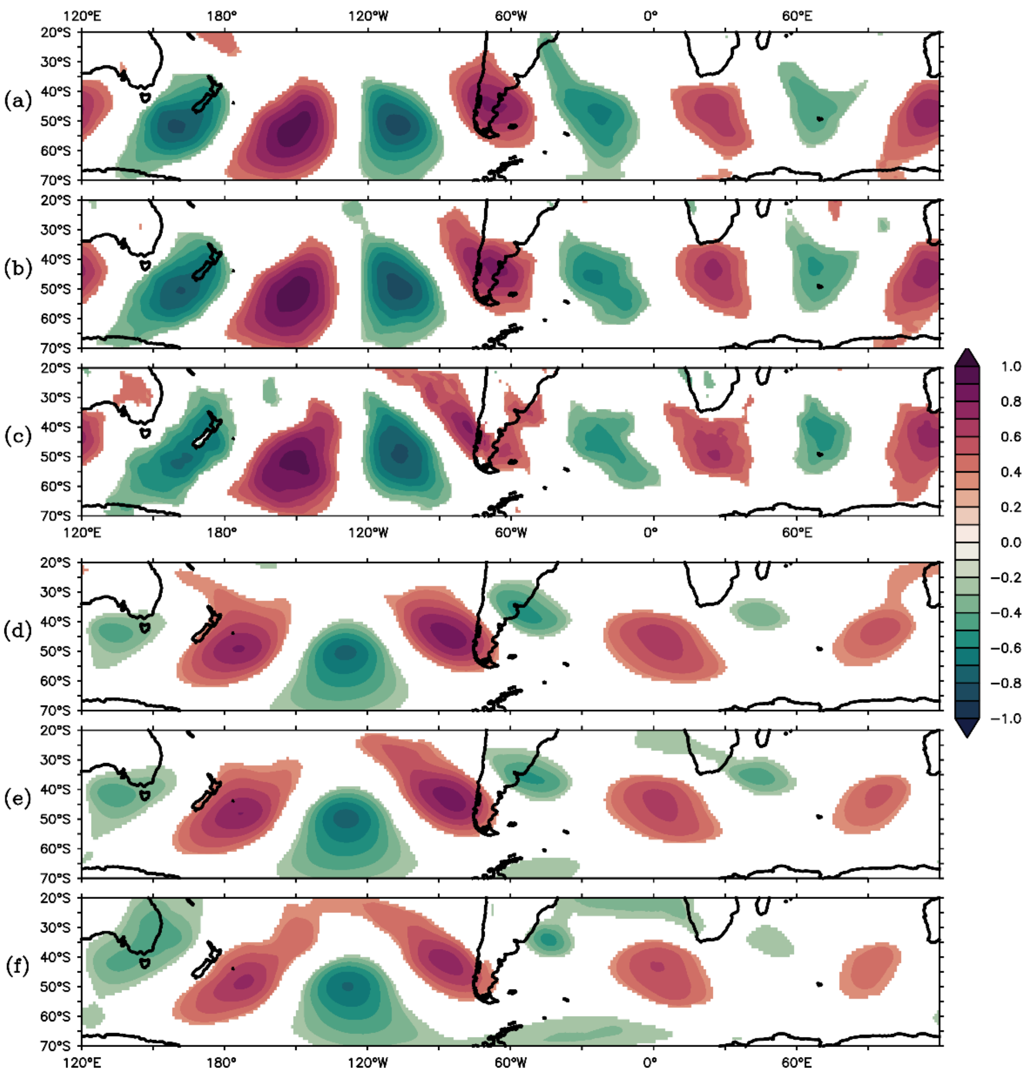


**Fig. 2** Correlation map of AW4 index with meridional wind anomalies at **(a)** 250 hPa, **(b)** 500 hPa, and **(c)** 850 hPa, and geo-potential height anomaly at **(d)** 250 hPa, **(e)** 500 hPa, and **(f)** 850 hPa. Values satisfying 95% significance using two-tailed t-test are shown.

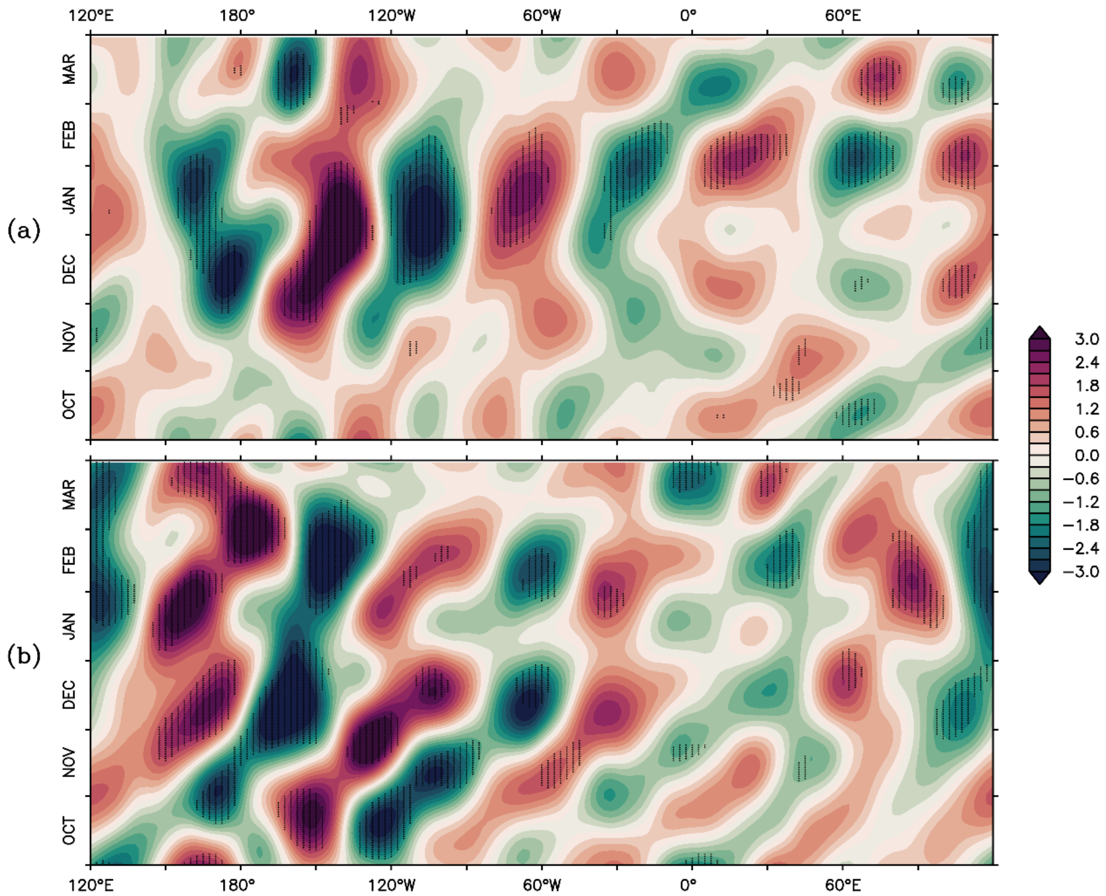


**Fig. 3** Hovmöller diagram (30°S-60°S averaged) of daily 250 hPa meridional wind anomaly during **(a)** positive years and **(b)** negative years. Values satisfying 90% significance using two tailed t-test are dotted.

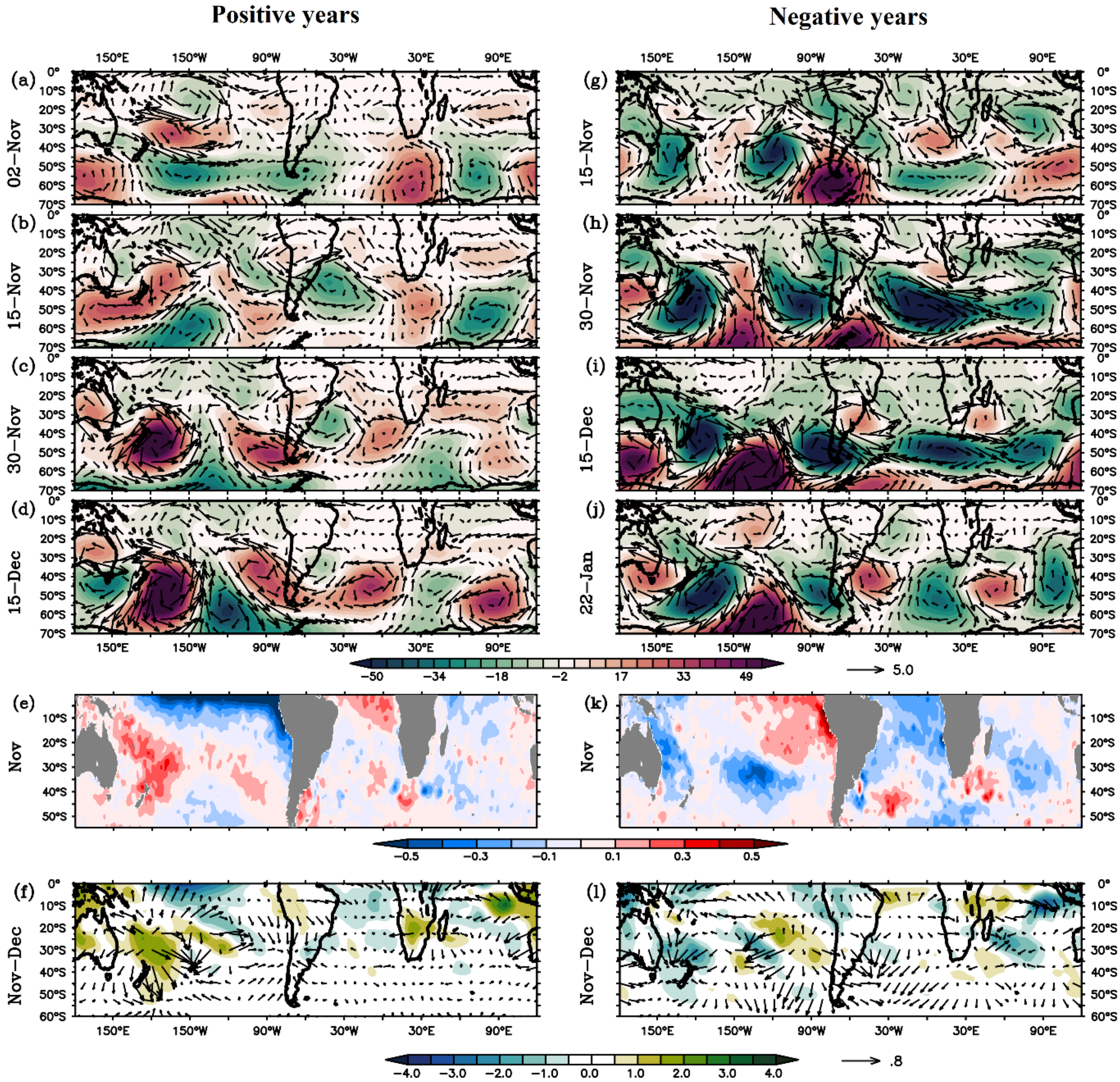


**Fig. 4** Left panel **(a-f)** Composite of daily geopotential height anomaly (filled in meter) and wind anomaly (vector in m/s) at 250 hPa for **(a)** 2nd November, **(b)** 15th November, **(c)** 30th November, and **(d)** 15th December during positive years. Composite of **(e)** November SST anomaly, and **(f)** November-December precipitable water anomaly (shaded in mm/day) and 250 hPa divergent wind (vector in m/s) during positive years. Right panel **(g-l)** is similar to left panel but for negative years.

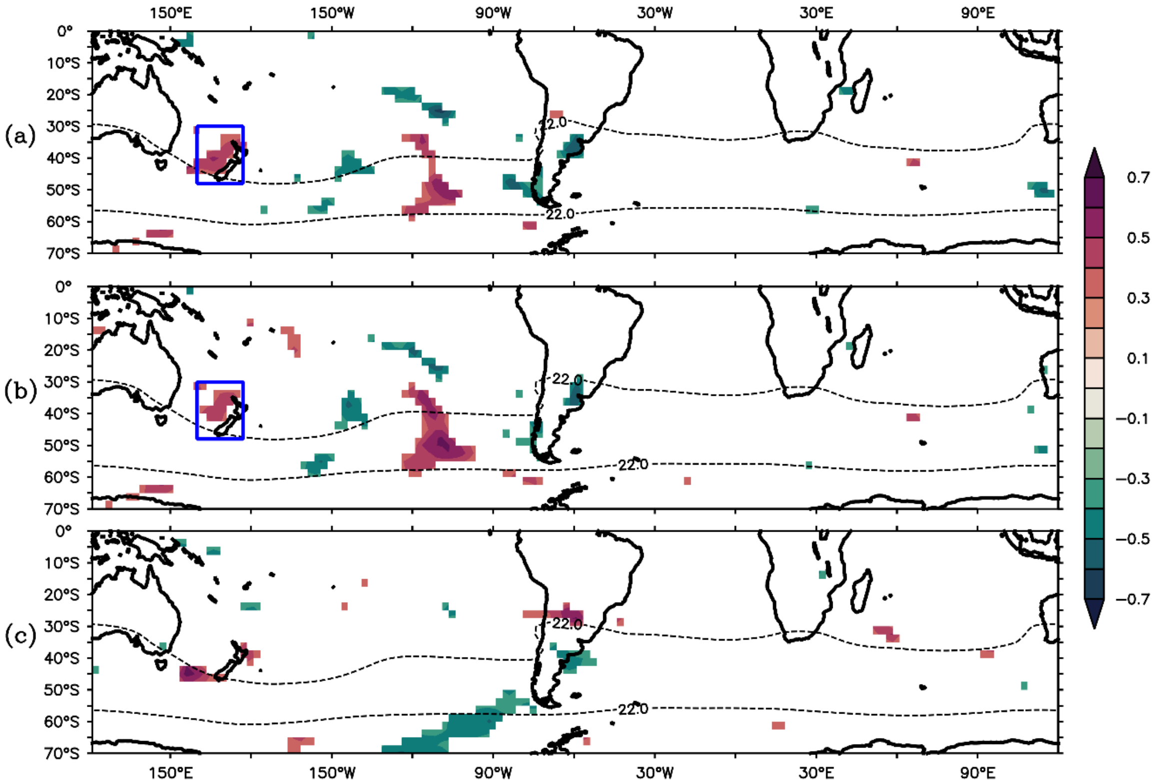


**Fig. 5** Correlation map of AW4 index and **(a)** RWS, **(b)** S1, and **(c)** S2 during austral summer. Values below 95% confidence interval using two tailed student's t-test are supressed. Dotted black line shows the westerly jet (contour of 22 m/s zonal wind). Blue box (160°E-177°E, 30°S-48°S) represents the potential region of RWS.

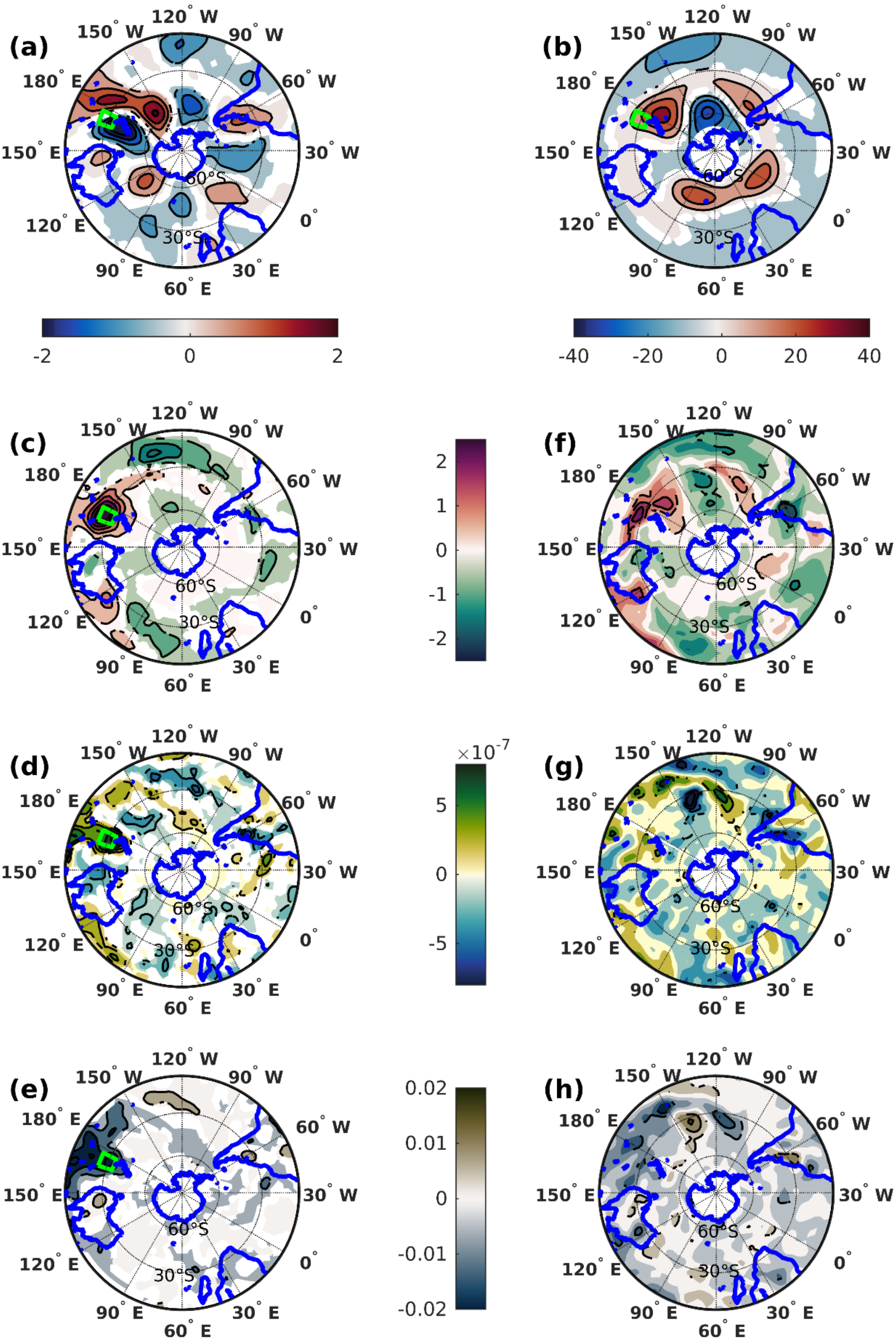


**Fig. 6** Linear step response function for 250 hPa anomalous **(a)** meridional wind **(b)** geopotential height **(c)** precipitable water (mm/day) **(d)** divergence ($s^{-1}$), and **(e)** 500 hPa vertical wind (pascal/sec), averaged over lag 30-40 days, forced by a 3 mm/day

area-averaged precipitable water anomaly over the region shown in green box, during DJF of 1979/80–2017/18. Shading is masked out using 1000 samples of first order auto-regressive red noise spectrum, and contour lines are only plotted where the step response function is more than 2 standard deviations of the red noise spectrum. Composite of **(f)** precipitable water anomaly (in mm/day) **(g)** 250 hPa divergence ($s^{-1}$), and **(h)** 500 hPa vertical wind (pascal/sec) during positive years (contour lines shows 90% significant values using two tailed t-test).

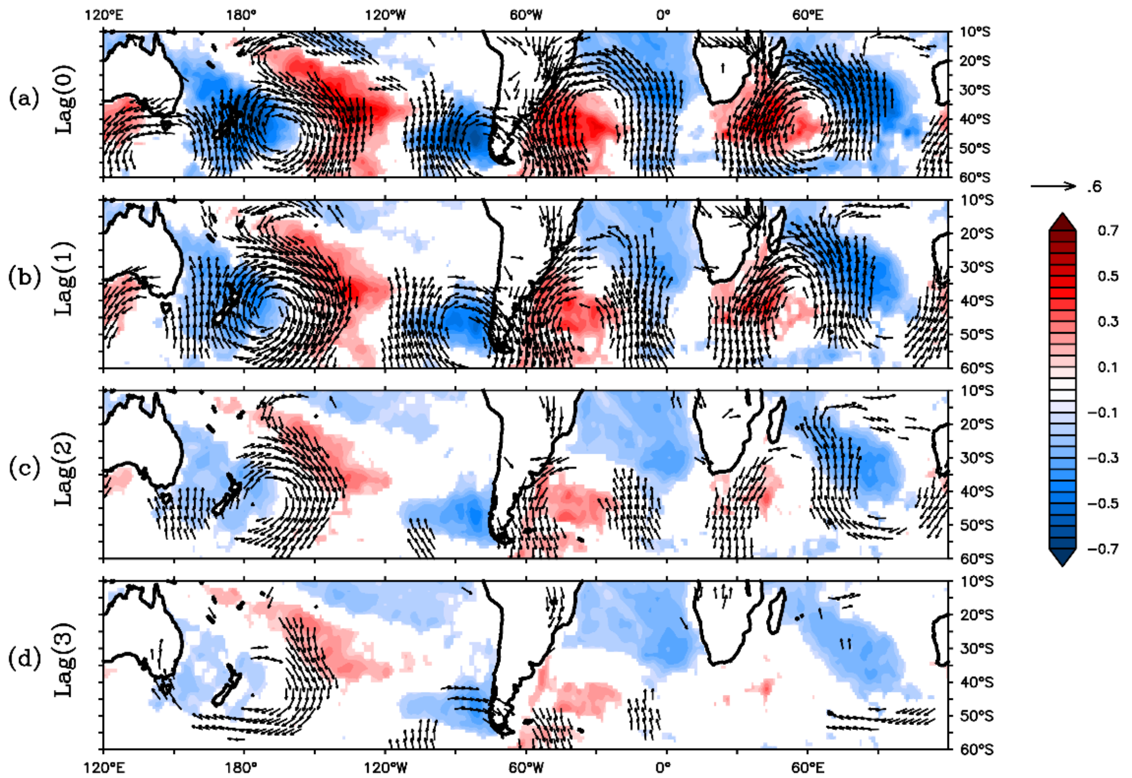


**Fig. 7** Lag cross-correlation between SST W4 index and SST anomaly (filled), and 850 hPa wind anomaly (vectors). Lag "1" stands for 1 month lagging of SST W4 index and so on. Areas not satisfying 99% significance using two tailed student's t-test are suppressed.

# Supplementary Information: Origin and dynamics of global atmospheric wavenumber-4 in the Southern mid-latitude during austral summer

**Balaji Senapati[1], Pranab Deb[1], Mihir K. Dash[1], and Swadhin K. Behera[2]**

[1]Centre for Oceans, Rivers, Atmosphere and Land Sciences, Indian Institute of Technology Kharagpur, Kharagpur, West Bengal, India.

[2]Application Laboratory, VAiG, Japan Agency for Marine-Earth Science and Technology, Yokohama, Kanagawa, Japan.

Corresponding author: Mihir K. Dash (mihir@coral.iitkgp.ac.in)

**Contents of this file**

Figure S1

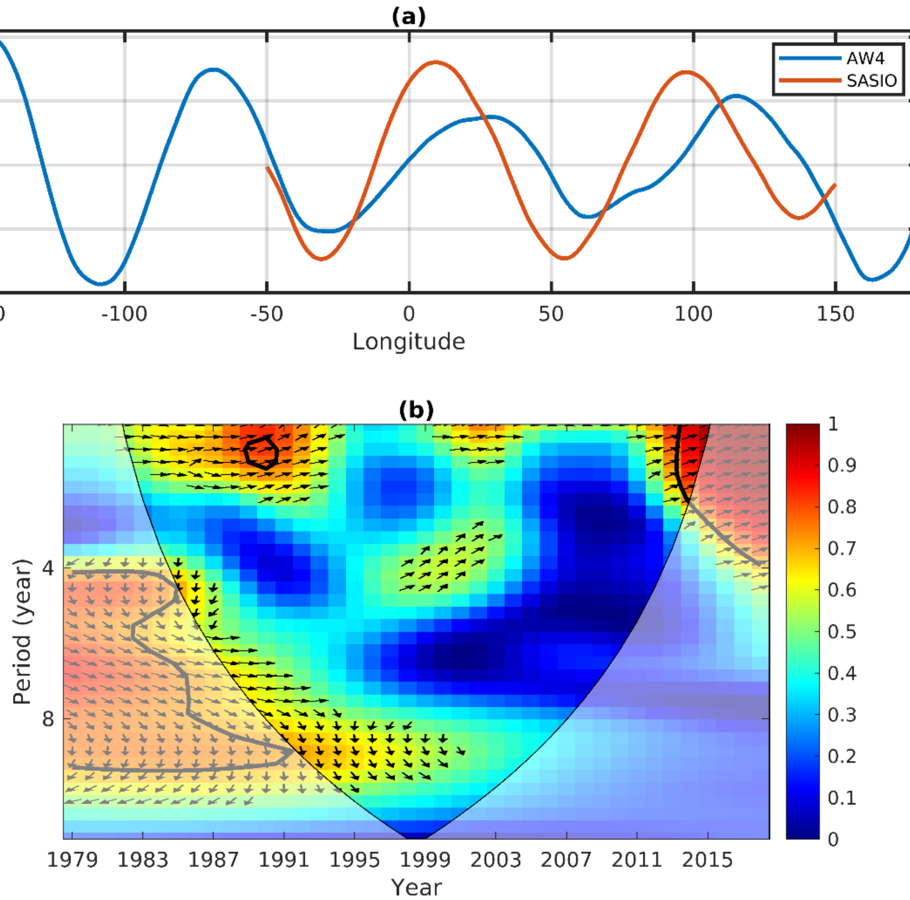

**Fig. S1 (a)** Meridional average of AW4 EOF pattern (blue line) and SASIO EOF pattern (red line). **(b)** The wavelet covariance and phase difference of AW4 index and SASIO time series in the cone of influence. Values higher than 95% confidence interval (using Monte-Carlo approach) are contoured with thick black line. Vectors pointing towards right (left) and down (up) represents the AW4 is in(out)-phase and leading (lagging) the SASIO by 90°. Vectors of lower covariance (less than 0.5) are suppressed.